Oxide-ion transport at low and high electric fields in brownmillerite $Sr_2Fe_2O_5$ and perovskite $SrFeO_{2.5}$: A molecular dynamics study

Sonja Ambaum,* Stine Spinger, and Roger A. De Souza†
Institute of Physical Chemistry, RWTH Aachen University, Landoltweg 2, 52074 Aachen, Germany

(Received 18 September 2025; accepted 27 January 2026; published 3 March 2026)

Strontium iron oxide undergoes a voltage-driven topotactic phase transition between an insulating brownmillerite (BM) and a conductive perovskite (PV) structure. Understanding this redox-based transition requires, first, a detailed characterization of and, second, a detailed description of field-driven oxide-ion transport in both phases. In this study, we used classical molecular dynamics (MD) simulations to determine the oxide-ion mobility u_{O} in anisotropic $Sr_2Fe_2O_{5\pm\delta}$ (BM phase) and in isotropic $SrFeO_{2.5\pm\delta/2}$ (PV phase) as a function of electric field strength, $0.5 \leqslant E/\mathrm{MV\,cm^{-1}} \leqslant 10$, and as a function of temperature, $1300 \leqslant T/\mathrm{K} \leqslant 3000$. The use of oxygen-excess ($+\delta$) and oxygen-deficient ($-\delta$) BM systems permits, respectively, interstitialcy and interstitial migration, and vacancy migration, to be probed. From u_{O} results obtained at low fields (i.e., within the linear regime), we obtain the activation enthalpies and effective attempt frequencies of oxygen-vacancy migration and oxygen-interstitial/oxygen-interstitialcy migration; and, together with literature data for tracer diffusivities, we determine Haven ratios $H_{\mathrm{r}}(T)$ for BM and PV phases. At higher fields (i.e., within the nonlinear regime), $u_{\mathrm{O}}(E)$ data shows a strong nonlinear response for all three migration mechanisms. In each case, the behavior is described within an existing analytical framework that uses as input the zero-field activation enthalpies and effective attempt frequencies. Interstitialcy migration displays a stronger nonlinear response compared with interstitial or vacancy migration, and this is ascribed to its longer effective charge displacement arising from its collective nature. Finally, the MD simulations at high field strengths indicate a field-driven BM-to-PV phase transition (at constant oxygen stoichiometry).

DOI: 10.1103/bwtd-x5cj

I. INTRODUCTION

Although they are derived from ABO_3 perovskites (PV), $A_2B_2O_5$ brownmillerites (BM) exhibit far more complex oxide-ion transport processes on account of their characteristic structural features. The anisotropic BM structure can be considered to consist of alternating layers of BO_6 octahedra and BO_4 tetrahedra [see Fig. 1(left)]. The main characteristic of the BO_4 layers is the arrangement of the corner-sharing BO_4 tetrahedra in chains with unoccupied "channels" separating these chains [see also Fig. 1(right, bottom)]. These channels are often termed "oxygen vacancy channels" (OVC) from a comparison with the disordered oxygen sublattice in the parent, cubic perovskite (PV) $ABO_{3-\delta}$ structure. Strictly speaking, however, they are neither channels of oxygen vacancies, nor channels for oxygen-vacancy migration. In fact, they are channels for oxygen interstitials, and so should be referred to as oxygen-interstitial channels (OIC).

Previous computational studies [1–5] focused on one-dimensional oxygen-interstitial migration along the OIC. In our recent study [6], we employed molecular dynamics (MD) simulations to examine in detail the mechanisms of oxide-ion migration in BM $Sr_2Fe_2O_5$. Our results indicate that oxide-ion diffusion takes place in two dimensions, both in the FeO_4 layers by means of interstitial and interstitialcy mechanisms and in the FeO_6 layers by means of a vacancy mechanism: It is certainly not confined to the OIC. In Fig. 1(right), we give an overview of the migration paths for vacancy and interstitial according to these MD simulations [6]. Although oxygen defects are relatively mobile in BM $Sr_2Fe_2O_5$, there are few defects present in equilibrium, and this results in low overall rates of oxygen diffusion.

In general, BM materials are electrically insulating at room temperature ($Sr_2Fe_2O_5$, for example, displaying a band gap of ca. 2 eV) [7]. However, they can undergo a reversible topotactic phase transition (i.e., without losing the lattice framework) to a cubic PV phase with high electrical conductivity (due to a partially filled band). The transition involves a rearrangement of the oxide ions that yields a perovskite structure with disordered, mobile oxygen vacancies. The contrast in resistance states between the BM and PV phases, along with the ability to induce the phase transition upon application of an electric field, makes BM oxides promising candidates for resistive-switching random access memory (ReRAM) [8–11] devices. Accordingly, the redox-based phase transition requires a detailed understanding of oxide-ion transport mechanisms in the BM phase. Given that migration processes and the phase transition occur under applied voltage in ReRAM devices, understanding how the field modifies these processes is important to thoroughly understand the switching behavior.

*Contact author: ambaum@pc.rwth-aachen.de
†Contact author: desouza@pc.rwth-aachen.de

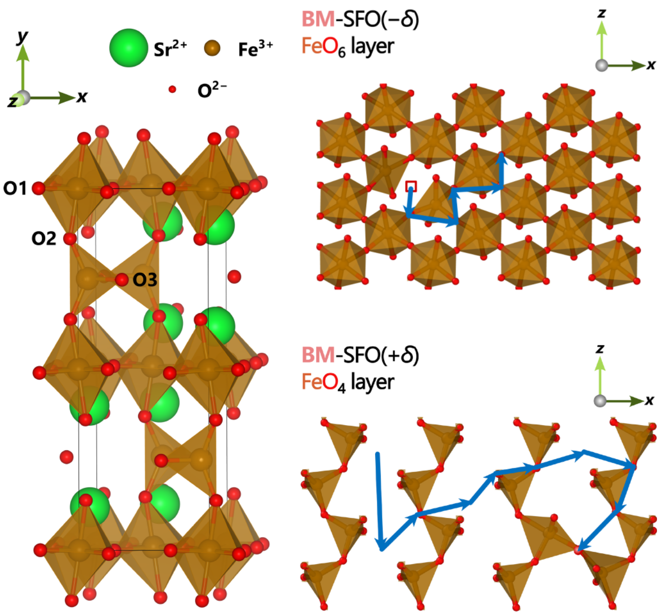

FIG. 1. (left) Unit cell of the orthorhombic *Ibm*2 structure of brownmillerite $Sr_2Fe_2O_5$, emphasizing the Fe–O polyhedra and the layered structure. The different oxygen sites (O1, O2, O3) in the brownmillerite structure are indicated. From previous MD simulations [6] obtained (right, top) jump vectors (blue) of oxide-ion vacancies in FeO_6 layers of oxygen-deficient SFO($-\delta$); and (right, bottom) jump vectors (blue) of interstitial oxide ions in FeO_4 layers of oxygen-excess SFO($+\delta$).

The main aims of this study were, therefore, to characterize, and then describe quantitatively, the effects of an electric field on oxide-ion transport in BM $Sr_2Fe_2O_5$ and PV $SrFeO_{2.5}$. To this end, we carried out, as a function of temperature and applied field, MD simulations with well-established empirical pair potentials (EPP) [12]. Compared with experiment, MD simulations offer the significant advantage of allowing the effects of an applied field to be considered, isolated from other effects: Experimental investigations of field-driven ion transport are challenging, since high electric fields may easily cause dielectric breakdown, Joule heating, and changes in (oxygen) stoichiometry (locally or globally) [13,14]. Compared with molecular static simulations, MD simulations offer the advantages of including finite-temperature effects, of yielding the ion mobility directly, and of allowing the system to decide which migration paths are taken. Classical MD allows us to use large system sizes and long timescales needed to quantify effects with reasonable statistical accuracy. In our previous study [6], we showed that the interatomic potentials used (see Sec. III) accurately reproduce vacancy diffusion coefficients in the PV phase of the $SrFeO_{3-\delta}$ system in agreement with experimental data.

We considered two systems, $Sr_2Fe_2O_{5.05}/SrFeO_{2.525}$ [SFO($+\delta$)], i.e., an oxygen-excess material relative to the stoichiometric BM; and $Sr_2Fe_2O_{4.95}/SrFeO_{2.475}$ [SFO($-\delta$)], i.e., an oxygen-deficient material. For the former, oxide ions were introduced into interstitial sites in the OIC in order to investigate the effect of a field on oxygen-interstitial transport; and for the latter, oxide ions were removed from equatorial sites in the FeO_6 layers in order to investigate the effect of a field on oxygen-vacancy transport (these sites corresponding to the energetically favored positions for the respective defect [6]). In the stoichiometric system $Sr_2Fe_2O_5$, both interstitials and vacancies will contribute to differing degrees to field-driven transport, and this of course would complicate the analysis of the data. Since the BM structure consists of layers, we considered oxide-ion transport in response to an applied field in two perpendicular directions within the FeO_4 and FeO_6 layers (along the x and z crystallographic directions). Transport along the y direction was not considered, since no transport perpendicular to the layers was observed in our previous study [6]. Fig. 1(right) summarizes the orientation of the field with respect to the jump vectors of the oxide ions.

II. PREDICTION OF $u_O(E)$

In seeking to describe quantitatively the oxide-ion mobility u_O as a function of field strength E and temperature T, we wanted specifically a simple, analytical description based only on zero-field parameters. This permits the prediction of the mobility for all relevant conditions, not just those considered in the simulations, and furthermore, for other BM systems, all with knowledge of only the appropriate zero-field quantities. The prediction of $u_i(E)$ dates back to the work of Verwey [15], Frenkel [16], and Mott and Gurney [17]. Their approach focused on how the electric field modifies the energy barriers for forward and reverse jumps of an ion of charge $|z_i|e$, and they assumed a superposition of a linear field term on the enthalpy hypersurface. While this approach successfully captures the field-independent behavior of u_i at low field strengths, as well as its increase at moderate field strengths, it overestimates the rise in u_i at high electric fields by underestimating the migration barrier in the direction of the applied field. It also produces physically unreasonable behavior, allowing the forward barrier to become negative at very high field strengths.

Genreith-Schriever and De Souza [14] developed a more accurate prediction of $u_i(E)$ by considering the (cosinusoidal) shape of the enthalpy landscape $H(x)$ along the migration coordinate x and, as before, superimposing a linear field term,

$$H(x) = \frac{\Delta H_{\mathrm{mig}}}{2}\left[1-\cos\left(\frac{2\pi x}{d_i}\right)\right] - |z_i|eEx, \quad (1)$$

where ΔH_{mig} is the activation enthalpy of migration at zero field. The migration enthalpies in forward (f) and reverse (r) jump direction follow as

$$\Delta H^{\mathrm{f/r}}_{\mathrm{mig}} = \Delta H_{\mathrm{mig}}\left[\sqrt{1-\gamma^2} \mp \gamma\left(\frac{\pi}{2}\right) + \gamma \arcsin\gamma\right], \quad (2)$$

with $\gamma = |z_i|eEd_i/(\pi\Delta H_{\mathrm{mig}})$ and d_i being the distance between the initial and final position of the jump process. This expression keeps the behavior of $\Delta H^{\mathrm{f}}_{\mathrm{mig}}$ physically reasonable: it goes to zero as γ approaches unity. The oxide-ion mobility is then obtained from

$$u_i = \frac{1}{E} n_{\mathrm{def}} d_i \nu_0 \exp\left(\frac{\Delta S_{\mathrm{mig}}}{k_{\mathrm{B}}}\right) \cdot \left[\exp\left(\frac{-\Delta H^{\mathrm{f}}_{\mathrm{mig}}}{k_{\mathrm{B}}T}\right) - \exp\left(\frac{-\Delta H^{\mathrm{r}}_{\mathrm{mig}}}{k_{\mathrm{B}}T}\right)\right], \quad (3)$$

where n_{def} is the defect site fraction, ν_0 is the (zero-field) attempt frequency, ΔS_{mig} is the (zero-field) activation entropy of migration and k_{B} the Boltzmann constant. In the limit of low field strengths, $E \ll 2k_{\mathrm{B}}T/(|z_i|ed_i)$, Eq. (3) becomes

$$\lim_{E\to 0} u_i = n_{\mathrm{def}} d_i^2 \frac{|z_i|e}{k_{\mathrm{B}}T}\nu_0 \exp\left(\frac{\Delta S_{\mathrm{mig}}}{k_{\mathrm{B}}}\right)\exp\left(\frac{-\Delta H_{\mathrm{mig}}}{k_{\mathrm{B}}T}\right), \quad (4)$$

i.e., field-independent behavior is recovered.

An additional aim of this study was to examine the relationship between this (low-field) oxide-ion mobility and the oxygen tracer diffusivity in the BM and PV systems. The Nernst–Einstein relation furnishes the conductivity diffusion coefficient D_i^σ from the (zero-field) mobility,

$$D_i^\sigma = \frac{k_{\mathrm{B}}T}{|z_i|e} u_i^{E\to 0}, \quad (5)$$

and it is related to the tracer diffusion coefficient D_i^* through the Haven ratio H_{r},

$$H_{\mathrm{r}} = \frac{D_i^*}{D_i^\sigma}. \quad (6)$$

For three-dimensional oxygen-vacancy migration in a cubic ABO_3 perovskite, Kemp and De Souza [18] derived $H_{\mathrm{r}} = f^*/(6/Z)$, where f^* is the tracer correlation factor and Z the number of surrounding ions that can jump into the vacancy. For a dilute solution of oxygen vacancies in a cubic perovskite, $f^* = 0.69$ [19] and $Z = 8$, so that $H_{\mathrm{r}} = 0.92$. This value was confirmed by Kemp and De Souza [18] through MD simulations of oxygen-vacancy transport with and without applied field.

In the treatments detailed above, the nominal charge of the mobile ion is used, and there are two reasons for this. First, various electrochemical methods indicate that the charge transported by a mobile ion in a crystalline solid corresponds to its formal charge [20]. Second, in the interatomic potentials employed, the ions' charge is set to their formal charge.

III. METHODS AND COMPUTATIONAL DETAILS

We performed MD simulations using the LAMMPS [21,22] software with the velocity Verlet algorithm for solving Newton's equations of motion. A Nosé–Hoover thermostat and barostat as implemented in the LAMMPS code with damping constants of 0.2 ps and 0.5 ps were used. The simulation cell consisted of $14 \times 14 \times 14$ unit cells of orthorhombic $Sr_2Fe_2O_5$ (space group $Ibm2$, see Ambaum *et al.* [6] for details about this choice and results section), containing a total of 98 784 ions. Excess charge arising from additional or missing oxide ions was compensated by modifying slightly the charge of all Fe ions. The simulations were conducted with periodic boundary conditions within the isothermal-isobaric (NpT) ensemble. The long-range Coulombic interactions were evaluated with a particle-particle particle-mesh solver [23] with an accuracy of 10^{-5}. Interatomic interactions Φ_{ij} were modeled as the sum of long-range Coulombic forces and short-range interactions described by a Buckingham potential:

$$\Phi_{ij}(r_{ij}) = \frac{q_i q_j}{4\varepsilon_0 r_{ij}} + A\exp^{-\frac{r_{ij}}{\rho_{ij}}} - \frac{C_{ij}}{r_{ij}^6}. \quad (7)$$

Here, q_i and q_j are the formal ion charges of ion i and j separated by distance r_{ij}; ε_0 is the vacuum permittivity; A, ρ_{ij}, and C_{ij} are empirical parameters, which were taken from Ford *et al.* [12]. These empirical potentials reproduce experimental crystallographic data (as they were fitted to such data [12]), and they yield diffusion data for PV $SrFeO_{2.5}$ in good agreement [6] with experimental diffusion data [24,25] (even though such data were not used in deriving the potentials).

Electric field strengths in the range of $0.5 \leqslant E/\mathrm{MV\,cm^{-1}} \leqslant 10$ were implemented in the simulations by applying an additional force $F = q_i eE$ to each particle. As elaborated by Kemp *et al.* [26], the tracer diffusion coefficient D_i^*, obtained by analyzing the ions' mean-squared displacement $\langle r_i^2\rangle$, is not the appropriate transport parameter to be extracted from MD simulations with an electric field, as it includes contributions from both diffusion and drift motion. Instead, the ions' mean displacement $\langle r_i\rangle$ should be monitored in order to determine the drift velocity v_{d} from which the ion mobility is obtained, $u_i = v_{\mathrm{d}}/E$. For improved statistics, two independent runs with different random seeds were performed for each combination of E and T.

IV. RESULTS AND DISCUSSION

In the BM structure, the ordering of the tilted tetrahedra in the tetrahedra chains along the z direction results in two different tetrahedra chain configurations with opposite polarization in the z direction. That is, the BM structure actually refers to a family of crystal structures that differ from one another by the orientation of these tetrahedra chains within each FeO_4 layer and between the FeO_4 layers. Experimental studies [27–29] and Density-Functional-Theory (DFT) calculations [30,31] show that the nonpolar $Pbma$ structure (with tetrahedra chains ordered that overall the polarization cancels out) is the thermodynamically most stable structure at zero field and room temperature. However, in this study and our previous one, we instead modeled the polar $Ibm2$ structure, in which the tetrahedra chains are all oriented in the same way. The reason for this choice is primarily that the potentials were derived for this structure. These potentials still reproduce correctly the energetic preference for the $Pbma$ structure [6]; however, the energy difference relative to the $Ibm2$ structure is minor ($\Delta E < 2$ meV per formula unit). Secondly, in the previous study [6] we observed that the tetrahedral chain ordering was dynamic at the temperatures considered in our MD simulations ($1300 \leqslant T/\mathrm{K} \leqslant T_{\mathrm{trs}}$), especially when interstitial ions had been inserted. Thus, the chain ordering of the initial structure had no significant influence on the oxide-ion diffusion or the phase transition. In the present study, however, an electric field is applied to a polar structure, and the relative orientation of the field and the polarization could still influence the results of this study. The DFT results of Arras *et al.* [31] show that the $Ibm2$ structure can be stabilized, or destabilized, relative to the nonpolar $Pbma$ structure when the field is applied parallel or antiparallel to the polarization, respectively. We performed, therefore, MD simulations with the electric field applied in either parallel (see Fig. S1 of the Supplemental Material (SM) [32]) or antiparallel orientations in the $Ibm2$ structure, and also, in a supercell based on the $Pbma$ structure (see Fig. S1 of the SM [32]). Effects on the

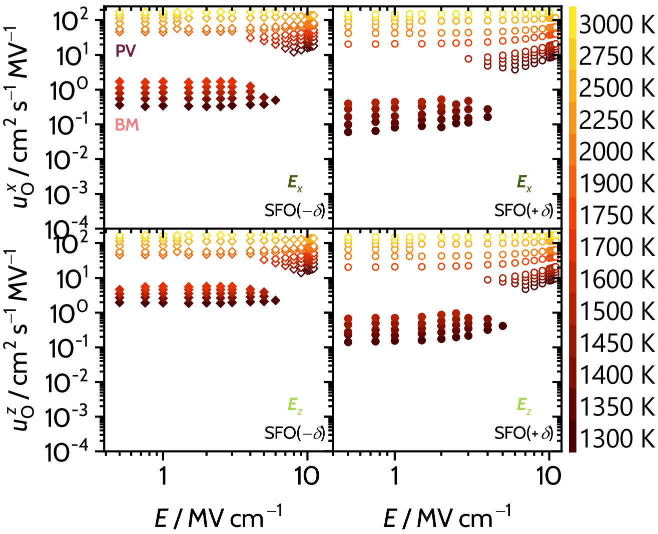

FIG. 2. Oxide-ion mobilities u_O as a function of electric field strength E applied in x and z directions obtained from MD simulation of oxygen-deficient SFO($-\delta$)(left) and oxygen-excess SFO($+\delta$)(right) in the range of $1300 \leqslant T/\mathrm{K} \leqslant 3000$. Closed symbols correspond to the BM phase, open symbols to the PV phase. Every data point is the average of two independent runs.

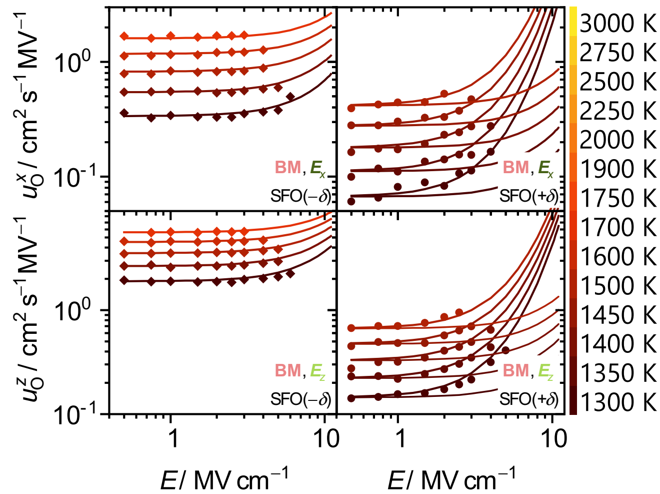

FIG. 3. Oxide-ion mobilities u_O as a function of electric field strength E applied in x and z directions obtained from MD simulation of oxygen-deficient SFO($-\delta$)(left) and oxygen-excess SFO($+\delta$)(right) in the BM phase. Solid lines are predictions of u_O according to Eq. (3) for the BM phase with d_O as average O–O distance in FeO_6 layers of the ideal, zero-kelvin cell for SFO($-\delta$) [$d_O = (a_{0\,K} + c_{0\,K})/4$ Å] and for d_O in SFO($+\delta$) an effective value of $d_O = 7.5$ Å is used. Semi-transparent lines show predictions of u_O with d_O as the average O–O distance in FeO_6 layers from the ideal cell for SFO($+\delta$).

phase transition are discussed in Sec. IV C. For the oxide-ion mobilities, no significant differences were observed for any orientation between field and polarization nor for the nonpolar structure, particularly with respect to the mainly qualitative conclusions we derive from the data of this study.

In order to confirm that no transport occurred in the y direction of the BM structure, we did perform a selected number of MD simulations, and we observed limited ion migration (with comparably poor statistics) only under conditions of very high field strengths and/or temperatures near the phase transition. Thus, we confirm that the focus in this study is appropriately on ion drift in the x and z directions.

In Fig. 2, we plot oxide-ion mobilities u_O for both nonstoichiometric systems, SFO($-\delta$) and SFO($+\delta$), for various temperatures as a function of applied electric field E in the x and the z directions (z: antiparallel to polarization). In both systems and in both directions, the data divides into two regimes. On the basis of lattice parameters and Fe coordination numbers, the data at lower temperatures and field strengths are found to correspond to the BM phase of these systems (filled symbols), whereas the data at higher temperatures and high field strengths are found to correspond to the PV phase (open symbols). Evidently, for all the systems considered, the phase transition from BM to PV shifts to lower temperatures with increasing field strength. We note, as found previously [6], that the phase-transition temperature (in simulations with these EPP) without an applied field is much higher than the experimental value [33–35]; and that this deviation is expected, since the potential parameters were not fitted [12] to reproduce the phase transition temperature. Furthermore, we note that the phase transition takes place at constant oxygen stoichiometry: it is driven by temperature or electric field. In the following three subsections we take a detailed look at the ion-transport behavior of each phase, and then at the phase transition.

A. $u_O(E, T)$ for BM

The oxide-ion mobilities u_O derived from MD simulations for the BM phase are shown in Fig. 3, offering a more detailed view on their directional and temperature-dependent behavior. For the oxygen-deficient system SFO($-\delta$), we find, for the range of temperature considered, that u_O is independent of field up to $E \approx 2$ MV cm^{-1} in both field directions, x and z.

In SFO($-\delta$), oxide-ion migration in x and z directions takes place by migration of oxygen vacancies [see Fig. 1(right, top)] between the equatorial sites of the FeO_6 layers of the BM structure [6]. The difference in u_O between the two directions, with higher values for the z than for the x direction accords well with the respective migration barriers, with a lower barrier for the z direction (0.67 eV) than for the x direction (0.77 eV), as found by climbing-image nudged elastic band (CI-NEB) calculations [6].

The oxygen-excess system SFO($+\delta$) shows field-independent ion mobilities up to $E \approx 1$ MV cm^{-1} for the range of temperature considered. Similar to SFO($-\delta$), an applied field in z direction results in higher ion mobilities than an applied field in x direction. The difference between the two field directions is, however, not as strong as in the SFO($-\delta$) system, which is in agreement with the smaller difference in the NEB migration barriers [6] between these two directions [x: (1.10 to 1.26) eV; z: (1.10 to 1.30) eV].

From the low-field regimes, we extract field-independent mobilities $u_O^{E\to 0}$, from which we calculate, with tracer diffusion data [6], the Haven ratio H_r; and from data as a function

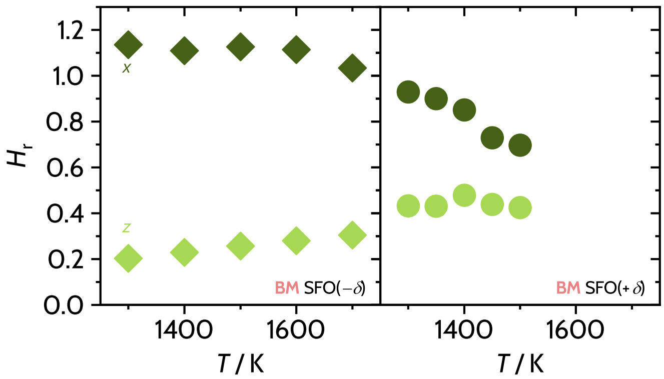

FIG. 4. Haven ratio H_r as a function of temperature T for both systems, (left) SFO($-\delta$) (diamonds) and (right) SFO($+\delta$) (cycles), in the BM phase from zero-field extrapolations in x (dark green) and z (light green) directions.

of temperature, the activation enthalpy of migration ΔH_{mig} and the effective jump frequency $\nu_0' = \nu_0 \exp(\Delta S_{mig}/k_B)$ (see Fig. S2 of the SM [36]). We begin by discussing the Haven ratio.

A value of $H_r = 1$ is commonly assumed when calculating ionic conductivities from tracer diffusion coefficients with Eq. (5). This assumption is rarely exactly correct, and it can be dangerous if H_r varies with temperature. Our results in Fig. 4 clearly demonstrate that the assumption of $H_r = 1$ does not hold for either oxygen-vacancy or oxygen interstitial migration in the brownmillerite structure investigated here. The values of H_r not only deviate significantly from unity but may also exhibit a dependence on temperature. H_r also depends strongly on the direction of the applied field in the system SFO($-\delta$), for which a vacancy mechanism is operative in both directions. Below we provide a qualitative explanation for the two main results, that (i) H_r is temperature-dependent and that (ii) H_r is direction-dependent.

Oxide-ion migration in the oxygen-deficient BM phase, according to our previous study [6], takes place exclusively by oxygen-vacancy migration between the equatorial sites of the PV-like FeO_6 layers [see Fig. 1(right, top)]. Given its similarity to the PV phase in terms of structure and migration mechanism, BM-SFO($-\delta$) may be first expected to display the same Haven ratio as that of cubic perovskite oxides. This simple consideration overlooks, however, three key factors: (i) the two-dimensional nature of migration; (ii) the unequal migration barriers in x and z directions; and (iii) the high vacancy concentration, which at $\approx$1 % is close to, if not already above, the dilute limit. The last aspect does not play a major role here, but it is discussed in detail in conjunction with the PV phase in Sec. IV B. Here, we focus on the first two, which in their combination result in, on the one hand, a temperature-dependent effective tracer correlation factor f^*_{eff} from D^*_O and, on the other hand, inequivalent effective jump frequencies for D^*_O and for u_O (thus D^σ_O), which both effect the Haven ratio.

We start with the temperature-dependent f^*_{eff}. To account for the two-dimensional character of vacancy migration within the PV-like FeO_6 layers, a first approximation is $H_r = f^*/(4/Z)$ (see Sec. II). According to this expression, any change in H_r arises from a change in either f^*, Z, or both. Since the coordination number Z is not temperature dependent, we attribute part of the temperature dependence of H_r to variations in f^*_{eff}.

For tracer diffusion on a two-dimensional lattice, Tahir-Kheli and El-Meshad [37] demonstrated that anisotropic migration barriers result in less strongly correlated jumps over the higher migration barrier (f^* is increased), whereas jumps over the lower migration barrier are more strongly correlated (f^* is decreased). Consequently, keeping the NEB [6] results in mind, that ΔE_{mig} in the x direction is higher than in the z direction for vacancy migration in the FeO_6 layers of $Sr_2Fe_2O_5$, we expect an increased value for f^* (and thus for H_r) in the x direction over the z direction. Our D^*_O values from zero-field MD simulations contain an effective f^* that evolves with temperature as the system transitions from predominantly one-dimensional migration along z (the low-barrier direction) to two-dimensional transport in the x–z plane. Thus, f^*_{eff} shifts gradually from a low-temperature value determined by the z direction to an effective value capturing contributions from both directions, leading to a temperature dependence in H_r.

This first approximation of $H_r = f^*/(4/Z)$ neglects, however, the second key aspect: the inequivalence of the effective jump frequencies ν_0' in the different crystallographic directions due to the different migration barriers. While the tracer diffusion coefficient D^*_O reflects an effective value over jumps in both the x and the z directions, the oxide-ion mobility u_O accounts only for jumps along the direction of the applied field. As a result, the effective jump frequency relevant for u_O differs from that in D^*_O and, hence, this expression for the Haven ratio [$H_r = f^*/(4/Z)$] cannot be derived. In fact, for the x direction, H_r even exceeds unity. Values of $H_r > 1$ have been reported [38–41], and they arise typically in nondilute or strongly correlated systems. This emphasizes that the handling of H_r is nontrivial. The Haven ratio cannot be easily estimated and the commonly assumed value of $H_r = 1$ is, at least in anisotropic systems, clearly invalid.

In the SFO($+\delta$) system, multiple migration pathways of the interstitial and interstitialcy mechanism with varying barriers exist along both the x and z directions. This complexity leads to differences in H_r between the two directions and contributes to its temperature dependence.

We now consider the second aspect of the low-field data, the behavior of $u_O^{E\to 0}$ as a function of temperature, in order to extract the migration barrier ΔH_{mig} and the effective jump frequency ν_0' [see Eq. (4)] for vacancies and interstitials in the x and the z directions. We plot $u_O^{E\to 0}T$ versus inverse temperature in Fig. 5 and find that $u_O^{E\to 0}T$ differs significantly in the BM phase for the two systems and field directions. In agreement with diffusion data from our previous study [6], vacancy migration in SFO($-\delta$) shows higher ion mobilities than interstitial and interstitialcy migration in SFO($+\delta$). The mobilities are higher in the z over the x direction especially for SFO($-\delta$), which is in agreement with the migration barriers (see below). The extracted migration barriers ΔH_{mig} are plotted in Fig. 6 and ΔH_{mig} is compared with reference data from previous work [6]. For the oxygen-deficient system BM-SFO($-\delta$), our field-dependent MD simulations of ΔH_{mig} show qualitative agreement with the NEB results [6]: the migration enthalpy ΔH_{mig} is higher in the x direction than in the z direction.

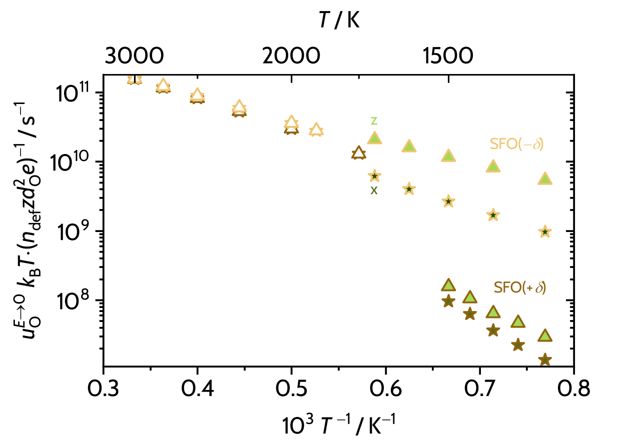

FIG. 5. $u_{\mathrm{O}}^{E\to 0}T$ as a function of inverse temperature T^{-1} for both systems, SFO($-\delta$) (light brown) and SFO($+\delta$) (dark brown), for the PV phase (open symbols) and the BM phase (filled symbols) from zero-field extrapolations in x (stars, dark green filled) and z (triangles, light green filled) directions.

Quantitatively, however, ΔH_{mig} of this study in the x direction differs from the NEB derived value. From NEB calculations, we obtain migration barriers that are unaffected by ion correlation phenomena. In contrast, our MD simulations capture correlated oxide-ion motion, particularly at low temperatures, as noted previously in the discussion of H_{r}. Thus, the probability of jumps in the x direction is reduced because of the highly correlated jumps in the lower-barrier z direction, especially at low temperatures and less in the high-temperature regime. This yields a higher migration barrier from MD than the NEB barrier. A similar explanation applies to the observation that the migration barrier from zero-field MD simulations [6] lies closer to the value obtained for the x direction. From zero-field MD simulations (i.e., obtaining D^*), only a single, effective migration barrier is extracted, which considers contributions from the migration barrier in the x and in the z directions, with different weighting depending on f_x^* and f_z^*. Thus, the effective zero-field migration barrier is lower than the migration barrier in x (as $\Delta H_{\mathrm{mig},x} > H_{\mathrm{mig},z}$) and higher than the migration barrier in z (as $f_x^* > f_z^*$).

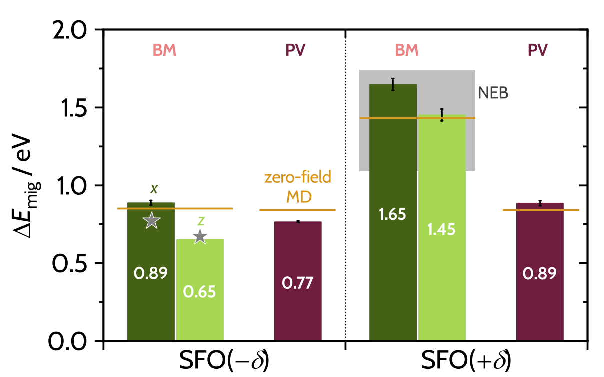

FIG. 6. Migration barriers ΔE_{mig} extracted from extrapolation of the low-field data [see Eq. (4)] for (left) vacancies and (right) interstitials in the x (dark green) and the z (light green) direction and for vacancies in the PV phase (purple). Reference data [6] from NEB (gray symbols and area) and zero-field MD simulations (light brown lines).

For the oxygen-excess system BM-SFO($+\delta$), our field-dependent MD results for ΔH_{mig} are consistent with NEB calculations [6], which show that interstitial and interstitialcy-like migration have higher migration barriers than the vacancy migration process. Here, the migration barrier from zero-field MD simulations [6] is closer to that of the z direction. According to H_{r} (see Fig. 4), f^* is similar for both directions. Thus, their weighting in the total migration barrier should rely only on ΔH_{mig} in each direction and the temperature. In this temperature regime, a value closer to the migration barrier in the z direction is expected. Overall, the migration barriers obtained from the field-dependent MD simulations show the same qualitative trend as both NEB calculations and zero-field MD simulations, with higher barriers for the interstitial/interstitialcy migration process in $Sr_2Fe_2O_5$.

Turning now from the low-field to the high-field behavior, we predict $u_{\mathrm{O}}(E,T)$ with Eq. (3), using these zero-field values of ΔH_{mig} and ν_0'. We consider the average distance between O ions in the FeO_6 layers of the ideal, zero-kelvin structure for d_{O} [$d_{\mathrm{O}} = (a_{0\,\mathrm{K}} + c_{0\,\mathrm{K}})/4$], but do not differentiate between the O–O distances in the two directions x and z. The predictions are shown in Fig. 3 as lines, and we find a good description for SFO($-\delta$) by the model (solid lines).

In the system SFO($+\delta$), the model (semi-transparent lines) does not describe the increase in u_{O} found in the BM phase at moderate field strengths, when we consider the same jump distance as for SFO($-\delta$). We examine two possibilities, having considered Eq. (3). First, we examine the possible generation of additional defects that increase n_{v} and, thus, the ion mobility [42]. For field strengths up to values that cause the phase transition, however, the effective anti-Frenkel barrier (according to the expression of Kemp and De Souza [42]) remains relatively high, resulting in the formation of less than one anti-Frenkel pair at these values of E and T (for enthalpy and entropy of formation $\Delta H_{\mathrm{aF}} = 7.2$ eV, $\Delta S_{\mathrm{aF}} = 30\ k_{\mathrm{B}}$ [6] and enthalpy of recombination of $\Delta H^{\mathrm{r}} = 0.3$ eV according to NEB calculations performed in the current study). The second possibility is that d_{O} differs from the crystallographic O–O distance. For oxygen-interstitial migration, there is the interstitial mechanism along the OIC with well-defined d_{O}, and also the interstitialcy mechanism, for which the displacement of a tracer (related to O–O distance) differs from the effective displacement of the charge and is a multiple of O–O. Considerations of both interstitial and interstitialcy jumps gives values between 5.3 Å and 7.9 Å, and we find increasing the jump distance to an effective value of $d_{\mathrm{O}} = 7.5$ Å yields good agreement with the data (solid lines). This result provides further evidence that the interstitialcy mechanism is important for O_i drift.

B. $u_{\mathrm{v}}(E,T)$ for PV

In the PV phase, we find differences in the temperature dependence of $u_{\mathrm{O}}^{E\to 0}T$ between the two systems, SFO($-\delta$) and SFO($+\delta$), as shown in Fig. 5. The discrepancy is most pronounced at lower temperatures and is reflected in the extracted migration barriers shown in Fig. 6, which differ between the two systems and from the value obtained from the

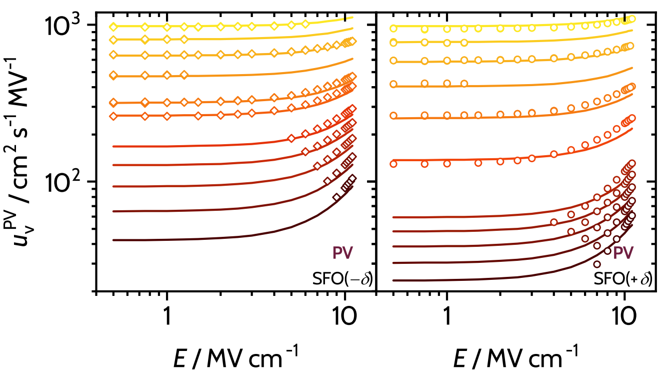

FIG. 7. Defect mobilities u_v^{PV} for oxygen vacancies as a function of electric field strength E obtained from MD simulation (left) of SFO($-\delta$) with higher vacancy concentration and (right) of SFO($+\delta$) with a bit lower vacancy concentration in the perovskite (PV) phase in the range of $1300 \leqslant T/\mathrm{K} \leqslant 3000$. For every E, there are two data points for applied field strengths in x and z direction. Lines are predictions of u_v according to Eq. (3) with O–O distance in the ideal, zero-kelvin cell.

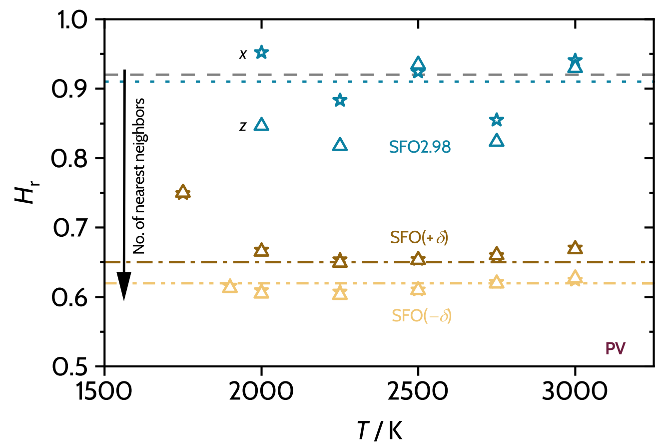

FIG. 8. Haven ratio H_r as a function of temperature T for both vacancy-concentrated systems, SFO($-\delta$) (light brown) and SFO($+\delta$) (dark brown), in the PV phase. Plotted also is the data for dilute-soluted SFO(2.98) (blue). The dashed gray line is H_r expected for cubic perovskites with dilute solution of oxygen vacancies, and the other dotted lines are the expected values when adapting the number of neighbors Z according to the vacancy concentrations of the systems. Triangles: electric field applied in x; stars: electric field applied in z.

D_O^* data [6] of both systems. In our previous study [6], defect diffusion coefficients $D_O^*/(f^* n_v)$ showed only minor differences between the two systems. However, when accounting for the different vacancy concentrations in the mobility data by looking at defect mobilities ($u_v = u_O/n_v$), see Fig. 7) rather than oxide-ion mobilities, we still find a difference between the two systems that is larger at lower temperatures. We attribute these discrepancies in the temperature behavior to the nonrandom distribution of vacancies in the PV phase, which varies with temperature, as shown in our previous study [6] and in the work of others [43]. Since the two systems have different vacancy distributions, also differences in the temperature dependence of u_v, respectively, $u_O^{E\to 0}$ are expected. With increasing temperature, we may expect a randomizing effect that gives us agreement between the two systems at higher temperatures. Diffusion captures the overall jumps in every direction, whereas u_O results from drift in only one direction. Consequently, u_O is more sensitive to the different vacancy distributions and we do not see this effect in the diffusion data.

When examining the Haven ratios in the PV phase (see Fig. 8), we find discrepancies also in H_r between the two systems. Starting from $H_r = f^*/(6/Z)$, this discrepancy in D_O^* and D_O^σ between the two systems has to be related to $(6/Z)$, since our earlier work [6] showed no difference in the defect diffusion coefficients between the two systems, implying that f^* is the same for both. A key feature of our systems are the high oxygen-vacancy site fractions, which at $\approx 17\,\%$ extend far beyond the dilute-solution limit. It is therefore reasonable to attribute discrepancies between the systems to differences in Z, and here we present two pieces of evidence. First, a substantial deviation of H_r from the expected value of 0.92 [18] for ABO_3 perovskites is found for our systems. However, reducing the vacancy site fraction to $\approx 0.67\,\%$ [SFO(2.98)] results in values of H_r close to the expected value. Second, an O–O coordination analysis yields coordination numbers of $Z = 7.95$ for SFO(2.98), $Z = 5.65$ for SFO($+\delta$), and $Z = 5.41$ for SFO($-\delta$). Using these values for Z to calculate the corresponding Haven ratios, we determine $H_r = 0.91$ [SFO(2.98)], $H_r = 0.65$ [SFO($+\delta$)], and $H_r = 0.62$ [SFO($-\delta$)] (shown as dashed lines in Fig. 8). These calculated values align surprisingly well with those obtained from the MD simulations and thus offer a simple explanation for both the deviations from the ideal value and the differences between the systems.

In Fig. 7, both nonstoichiometric systems show constant isothermal values of u_v up to $E \approx 3\,\mathrm{MV\,cm^{-1}}$ at the temperatures considered. Above this value, the vacancy mobilities increase with increasing field strength; this effect is stronger at lower temperatures. The model [Eq. (3)] fails to describe the increase of the ion mobility accurately. We attribute this to a deformation of the simulation cell at these high fields (see Fig. S3 of the SM [44]), as this is not considered in the model. Moreover, a discrepancy between data and model is found at lower temperatures. The values for $u_O^{E\to 0}$ were extracted from an extrapolation of $u_O^{E\to 0}$ from higher temperatures, since no data at low field strengths in the PV phase is available for a prediction of $u_O^{E\to 0}$. At these low temperatures, however, the model does not even capture the data at lower field strengths $E < 5\,\mathrm{MV\,cm^{-1}}$, particularly for the SFO($+\delta$) system. We assume this to be related to the temperature dependence of the nonrandom vacancy distributions.

C. E_{trs} for BM-to-PV phase transition

Previous studies [33,45–48] of the BM-to-PV phase transition as a function of temperature and oxygen partial pressure highlighted the redox-based character of the transition. In this study, however, we found a depression of the phase-transition temperature as a function of the electric field strength at constant oxygen stoichiometry. In seeking to describe this behavior, we start from the Gibb's free energy for dielectrics,

$$dG = V\,dp - S\,dT - VD\,dE, \tag{8}$$

where D is the dielectric displacement. For polar dielectrics, such as the *Ibm*2 structure, D consists of two terms, $D = \epsilon_0\epsilon_r E + P^0$, with ϵ_0 being the vacuum permittivity and ϵ_r being the relative dielectric permittivity. The first term, $\epsilon_0\epsilon_r E$, gives the induced polarization in response to the field, while the second term P^0 is the spontaneous polarization at zero field. In general, P^0 complicates the thermodynamic treatment of the phase transition.

In our simulations, however, we observe that the orientation of the electric field relative to the polarization does not significantly affect the phase transition temperature, neither for SFO($+\delta$) in either field direction nor for SFO($-\delta$) with the field applied along the x direction. Minor deviations might be detectable, particularly for SFO($-\delta$) with the field applied in the z direction, between the two orientations and in comparison to the nonpolar *Pbma* structure. In principal, we expect an influence of the polarization only with a field applied in z direction as the polarization is oriented only along the tetrahedra chains, thus in z direction. For SFO($+\delta$), similar phase transition behavior is expected, given the dynamic rearrangement of tetrahedral chain configurations that is found for this system with interstitial ions at elevated temperatures [6]. For SFO($-\delta$), prior DFT results of Arras *et al.* [31] suggest that the *Ibm*2 structure with the field aligned parallel to the polarization should be energetically favored over both the antiparallel orientation and the nonpolar *Pbma* structure. Due to the statistical fluctuations in the phase transition temperature, our data does not allow for an identification of any trend.

Any differences between the two BM structures considered and the orientation of field and polarization are minor in comparison to the differences in the thermodynamics of the two phases, BM and PV, especially relevant for the phase transition. Therefore, we neglect P^0 and proceed with the simplified description, $D = \epsilon_0\epsilon_r E$. For the case of constant pressure p, we then obtain

$$\frac{dE}{dT} = -\frac{1}{\epsilon_0}\frac{(S_{\rm PV} - S_{\rm BM})}{(V_{\rm PV}\epsilon_{\rm r,PV} - V_{\rm BM}\epsilon_{\rm r,BM})}\frac{1}{E}, \tag{9}$$

where S is the entropy of the respective phase and V the volume. This is essentially a variant of the Clapeyron equation. Substituting ΔS by $\Delta H/T$ in Eq. (9) and integrating, assuming the quantities ΔH, $\Delta\epsilon_r$, ΔV to be temperature- and field-independent, we find:

$$E_{\rm trs}^2 = -\frac{1}{\epsilon_0}\frac{\Delta H}{\Delta(V\epsilon_r)}\cdot \ln\left(\frac{T_{\rm trs}}{T_{\rm trs}^{E\to 0}}\right). \tag{10}$$

Extracting the field strength $E_{\rm trs}$ and the temperature $T_{\rm trs}$ at which the phase transition occurs from Fig. 2, we thus plot $E_{\rm trs}^2$ versus $\ln(T_{\rm trs}/T_{\rm trs}^{E\to 0})$ for each field direction and both systems in Fig. 9.The plot shows the expected linear behavior for both systems and each field direction. Linear regression of the data yields extrapolations that intersect the x axis and y axis close to the origin, as required by the thermodynamic treatment. This linear behavior and the good agreement of the intersection supports the thermodynamic nature of this E- and T-induced phase transition and supports our assumption that P^0 is of minor relevance for the phase transition.

For each field direction, the SFO($-\delta$) system requires consistently higher field strengths and temperatures for the phase transition than the SFO($+\delta$) system, indicating the stabilizing effects of higher oxygen deficiencies for the BM phase. Additionally, within each system, an electric field applied in the z direction induces the phase transition at lower E and T than for a field applied along the x direction. Deviations between the two directions are expected because of the anisotropic nature of the BM phase.

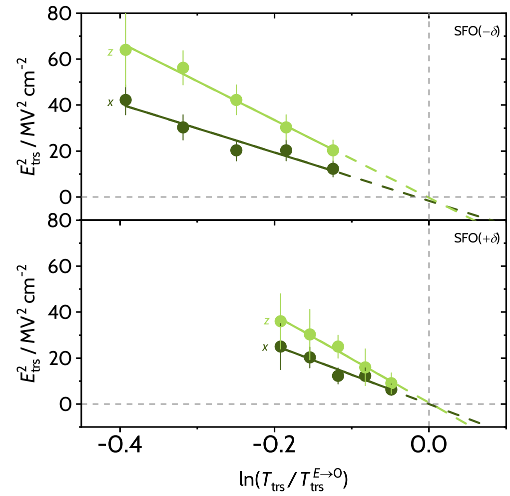

FIG. 9. Field strength of BM-to-PV phase transition $E_{\rm trs}^2$ as a function of $\ln(T_{\rm trs}/T_{\rm trs}^{E\to 0})$ of the phase transition temperature for both systems, (top) SFO($-\delta$) and (bottom) SFO($+\delta$).

Although the overall form of the data agrees well with Eq. (9), we were unable to reproduce the numerical value of the prefactor $-\Delta H/[\epsilon_0\Delta(V\epsilon_r)]$, using zero-field parameters and dielectric tensors obtained from static lattice simulations (with GULP, see Table S1 of the SM [49]), in agreement with the slopes obtained from the linear regressions. Even small variations, for example in ϵ_r, can lead to significant differences in the prefactor. In fact, ϵ_r is assumed to be constant but may vary significantly at these high field strengths. At present, it remains unclear whether the discrepancy between the theoretical prefactor and the values obtained from the linear regressions arises from limitations of our field-dependent MD simulations or from the nontrivial behavior of the prefactor's parameters with field. However, the clear linear trends observed in our data suggest that the thermodynamic description captures the essential physics of the field-induced phase transition.

V. CONCLUSIONS

In this study, we quantitatively analyzed the effect of an electric field on oxide-ion transport in both brownmillerite BM $Sr_2Fe_2O_5$ and perovskite PV $SrFeO_{2.5}$ within an established analytical framework. Our results highlight the significantly stronger nonlinear response of multi-ion migration mechanisms compared to single-particle processes, which we attribute to greater displacement of charge per jump event. In addition, we extracted Haven ratios from the simulations for both BM and PV phases. In the BM phase, a nontrivial behavior of the Haven ratio was found that depends on the migration mechanism and applied field direction. In the PV phase, the reduced number of nearest neighbors in highly oxide-ion defective systems affect the ion mobilities. For both phases, the extracted Haven ratios deviate significantly from the ideal value of one and vary as a function of temperature, indicating that this common assumption to convert between diffusivity and conductivity may not hold for every oxide material. Finally, our findings demonstrate that an applied electric field itself induces a BM-to-PV phase transition, even in the absence of accompanying changes in oxygen stoichiometry typically observed in experiments.

ACKNOWLEDGMENTS

Funding from the German Research Foundation (DFG) under Project No. 505655178 is gratefully acknowledged. Computations were performed with computing resources granted by RWTH Aachen University under project rwth1246 and rwth1602. The authors gratefully acknowledge the computing time provided to them at the NHR Center NHR4CES at RWTH Aachen University (Project No. p0020441). This is funded by the Federal Ministry of Education and Research, and the state governments participating on the basis of the resolutions of the GWK for national high performance computing at universities [50].

DATA AVAILABILITY

The data that support the findings of this article are not publicly available. The data are available from the authors upon reasonable request.

[1] W. Paulus, H. Schober, S. Eibl, M. Johnson, T. Berthier, O. Hernandez, M. Ceretti, M. Plazanet, K. Conder, and C. Lamberti, Lattice dynamics to trigger low temperature oxygen mobility in solid oxide ion conductors, J. Am. Ceram. Soc. **130**, 16080 (2008).

[2] C. Mitra, T. Meyer, H. N. Lee, and F. A. Reboredo, Oxygen diffusion pathways in brownmillerite $SrCoO_{2.5}$: Influence of structure and chemical potential, J. Chem. Phys. **141**, 084710 (2014).

[3] Q. Zhang, G. Hu, V. Starchenko, G. Wan, E. M. Dufresne, Y. Dong, H. Liu, H. Zhou, H. Jeen, K. Saritas, J. T. Krogel, F. A. Reboredo, H. N. Lee, A. R. Sandy, I. C. Almazan, P. Ganesh, and D. D. Fong, Phase transition dynamics in a complex oxide heterostructure, Phys. Rev. Lett. **129**, 235701 (2022).

[4] M. Alaydrus, I. Hamada, and Y. Morikawa, Mechanistic insight into oxygen vacancy migration in $SrFeO_{3\delta}$ from DFT + U simulations, Phys. Chem. Chem. Phys. **23**, 18628 (2021).

[5] U. Matsumoto, A. Kuwabara, C. A. J. Fisher, H. Moriwake, and I. Tanaka, Oxide-ion diffusion in brownmillerite-type $Ca_2AlMnO_{5+\delta}$ from first-principles calculations, Phys. Chem. Chem. Phys. **24**, 1503 (2022).

[6] S. Ambaum, N. L. Allan, R. Dittmann, and R. A. De Souza, Oxygen diffusion in brownmillerite $Sr_2Fe_2O_5$ is two-dimensional: Results from a molecular dynamics study, Chem. Mater. **36**, 2039 (2024).

[7] V. L. Kozhevnikov, I. A. Leonidov, M. V. Patrakeev, E. B. Mitberg, and K. R. Poeppelmeier, Electrical properties of the ferrite $SrFeO_y$ at high temperatures, J. Solid State Chem. **158**, 320 (2001).

[8] S. K. Acharya, J. Jo, N. V. Raveendra, U. Dash, M. Kim, H. Baik, S. Lee, B. H. Park, J. S. Lee, S. C. Chae, C. S. Hwang, and C. U. Jung, Brownmillerite thin films as fast ion conductors for ultimate-performance resistance switching memory, Nanoscale **9**, 10502 (2017).

[9] V. R. Nallagatla, T. Heisig, C. Baeumer, V. Feyer, M. Jugovac, G. Zamborlini, C. M. Schneider, R. Waser, M. Kim, C. U. Jung, and R. Dittmann, Topotactic phase transition driving memristive behavior, Adv. Mater. **31**, 1903391 (2019).

[10] V. R. Nallagatla and C. U. Jung, Resistive switching behavior in epitaxial brownmillerite $SrFeO_{2.5}/Nb:SrTiO_3$ heterojunction, Appl. Phys. Lett. **117**, 143503 (2020).

[11] S. K. Acharya, R. V. Nallagatla, O. Togibasa, B. W. Lee, C. Liu, C. U. Jung, B. H. Park, J.-Y. Park, Y. Cho, D.-W. Kim, J. Jo, D.-H. Kwon, M. Kim, C. S. Hwang, and S. C. Chae, Epitaxial brownmillerite oxide thin films for reliable switching memory, ACS Appl. Mater. Interfaces **8**, 7902 (2016).

[12] L. J. Ford, P. R. Slater, J. K. Christie, and P. Goddard, Carbon dioxide and water incorporation mechanisms in $SrFeO_{3-\delta}$ phases: A computational study, Phys. Chem. Chem. Phys. **22**, 25146 (2020).

[13] S. Murugavel and B. Roling, Application of nonlinear conductivity spectroscopy to ion transport in solid electrolytes, J. Non-Cryst. Solids **351**, 2819 (2005), Proceedings of 3rd International Conference on Broadband Dielectric Spectroscopy and Its Applications.

[14] A. R. Genreith-Schriever and R. A. De Souza, Field-enhanced ion transport in solids: Re-examination with molecular dynamics simulations, Phys. Rev. B **94**, 224304 (2016).

[15] E. J. W. Verwey, Electrolytic conduction of a solid insulator at high fields The formation of the anodic oxide film on aluminium, Physica **2**, 1059 (1935).

[16] J. Frenkel, *Kinetic Theory Of Liquids* (Oxford University Press, Oxford, UK, 1946).

[17] S. N. F. Mott and R. W. Gurney, *Electronic Processes in Ionic Crystals*, 2nd ed. (Oxford University Press, Oxford, 1948).

[18] D. Kemp and R. A. De Souza, Nonlinear ion mobility at high electric field strengths in the perovskites $SrTiO_3$ and $CH_3NH_3PbI_3$, Phys. Rev. Mater. **5**, 105401 (2021).

[19] T. Ishigaki, S. Yamauchi, K. Kishio, J. Mizusaki, and K. Fueki, Diffusion of oxide ion vacancies in perovskite-type oxides, J. Solid State Chem. **73**, 179 (1988).

[20] R. A. De Souza and D. N. Mueller, Electrochemical methods for determining ionic charge in solids, Nat. Mater. **20**, 443 (2021).

[21] S. Plimpton, Fast parallel algorithms for short-range molecular dynamics, J. Comput. Phys. **117**, 1 (1995).

[22] A. P. Thompson, H. M. Aktulga, R. Berger, D. S. Bolintineanu, W. M. Brown, P. S. Crozier, P. J. Veld, A. Kohlmeyer, S. G. Moore, T. D. Nguyen, R. Shan, M. J. Stevens, J. Tranchida, C. Trott, and S. J. Plimpton, LAMMPS—a flexible simulation tool for particle-based materials modeling at the atomic, meso, and continuum scales, Comput. Phys. Commun. **271**, 108171 (2022).

[23] R. W. Hockney and J. W. Eastwood, *Computer Simulation using Particles* (Taylor & Francis Group, New York, 1988).
[24] L. Wang, R. Merkle, and J. Maier, Surface kinetics and mechanism of oxygen incorporation into $Ba_{1-x}Sr_xCo_yFe_{1-y}O_{3-d}$ SOFC microelectrodes, J. Electrochem. Soc. **157**, B1802 (2010).
[25] J. Yoo and A. J. Jacobson, A study of the oxygen transport kinetics in $SrFeO_{3-x}$, MRS Proc. **756**, 310 (2002).
[26] D. Kemp, A. Tarancón, and R. A. De Souza, Recipes for superior ionic conductivities in thin-film ceria-based electrolytes, Phys. Chem. Chem. Phys. **24**, 12926 (2022).
[27] J. E. Auckett, A. J. Studer, N. Sharma, and C. D. Ling, Floating-zone growth of brownmillerite $Sr_2Fe_2O_5$ and the observation of a chain-ordered superstructure by single-crystal neutron diffraction, Solid State Ionics **225**, 432 (2012).
[28] J. E. Auckett, A. J. Studer, E. Pellegrini, J. Ollivier, M. R. Johnson, H. Schober, W. Miiller, and C. D. Ling, Combined experimental and computational study of oxide ion conduction dynamics in $Sr_2Fe_2O_5$ brownmillerite, Chem. Mater. **25**, 3080 (2013).
[29] M. Batuk, D. Vandemeulebroucke, M. Ceretti, W. Paulus, and J. Hadermann, Topotactic redox cycling in $SrFeO_{2.5+\delta}$ explored by 3D electron diffraction in different gas atmospheres, J. Mater. Chem. A **11**, 213 (2022).
[30] J. Young and J. M. Rondinelli, Crystal structure and electronic properties of bulk and thin film brownmillerite oxides, Phys. Rev. B **92**, 174111 (2015).
[31] R. Arras, C. Paillard, and L. Bellaiche, Effect of an electric field on ferroelectric and piezoelectric properties of brownmillerite $Ca_2Al_2O_5$, Phys. Rev. B **107**, 144107 (2023).
[32] See Supplemental Material at http://link.aps.org/supplemental/10.1103/bwtd-x5cj for a comparison of ion mobilities with the electric field applied parallel and antiparallel to the polarization of the *Ibm*2 structure, as well as for simulations of the nonpolar *Pbma* structure.
[33] J.-C. Grenier, N. Ea, M. Pouchard, and P. Hagenmuller, Structural transitions at high temperature in $Sr_2Fe_2O_5$, J. Solid State Chem. **58**, 243 (1985).
[34] M. Schmidt and S. J. Campbell, Crystal and magnetic structures of $Sr_2Fe_2O_5$ at elevated temperature, J. Solid State Chem. **156**, 292 (2001).
[35] S. Shin, M. Yonemura, and H. Ikawa, Crystallographic properties of $Ca_2Fe_2O_5$. Difference in crystallographic properties of brownmillerite-like compounds, $Ca_2Fe_2O_5$ and $Sr_2Fe_2O_5$, at elevated temperatures, Bull. Chem. Soc. Jpn. **52**, 947 (1979).
[36] See Supplemental Material at http://link.aps.org/supplemental/10.1103/bwtd-x5cj for effective jump frequencies of the BM and the PV phase.
[37] R. A. Tahir-Kheli and N. El-Meshad, Correlated diffusion in two-dimensional systems, Phys. Rev. B **32**, 6166 (1985).
[38] G. E. Murch, Diffusion in highly defective solids the Haven ratio in the athermal lattice gas, Philos. Mag. A **41**, 701 (1980).
[39] M. C. Lonergan, J. W. Perram, M. A. Ratner, and D. F. Shriver, Monte Carlo investigations of Coulombic correlations in lattice gas models, J. Chem. Phys. **98**, 4937 (1993).
[40] F. Wilangowski and N. A. Stolwijk, A Monte Carlo study of ionic transport in a simple cubic random alloy via the interstitialcy mechanism: Effects of noncollinear and direct interstitial jumps, Philos. Mag. **97**, 108 (2017).
[41] F. Hergemöller and N. A. Stolwijk, Monte Carlo simulation of correlation effects in a random SC alloy via interstitialcy mechanisms, Diffusion Foundations **19**, 35 (2019).
[42] D. Kemp and R. A. De Souza, One stone, two birds: Using high electric fields to enhance the mobility and the concentration of point defects in ion-conducting solids, J. Am. Chem. Soc. **146**, 4783 (2024).
[43] E. Bakken, N. L. Allan, T. H. K. Barron, C. E. Mohn, I. T. Todorov, and S. Stølen, Order-disorder in grossly nonstoichiometric $SrFeO_{2.50}$—a simulation study, Phys. Chem. Chem. Phys. **5**, 2237 (2003).
[44] See Supplemental Material at http://link.aps.org/supplemental/10.1103/bwtd-x5cj for a plot of the cell parameter as a function of field strength.
[45] J. Cheng, A. Navrotsky, X.-D. Zhou, and H. U. Anderson, Thermochemistry of $La_{1-x}Sr_xFeO_{3-\delta}$ solid solutions ($0.0 \leqslant x \leqslant 1.0, 0.0 \leqslant \delta \leqslant 0.5$), Chem. Mater. **17**, 2197 (2005).
[46] I. Starkov, S. Bychkov, A. Matvienko, and A. Nemudry, Oxygen release technique as a method for the determination of "$\delta - pO_2 - T$" diagrams for MIEC oxides, Phys. Chem. Chem. Phys. **16**, 5527 (2014).
[47] J. Mizusaki, M. Okayasu, S. Yamauchi, and K. Fueki, Nonstoichiometry and phase relationship of the $SrFeO_{2.5}-SrFeO_3$ system at high temperature, J. Solid State Chem. **99**, 166 (1992).
[48] Y. Takeda, K. Kanno, T. Takada, O. Yamamoto, M. Takano, N. Nakayama, and Y. Bando, Phase relation in the oxygen nonstoichiometric system, $SrFeO_x (2.5 \leqslant x \leqslant 3.0)$, J. Solid State Chem. **63**, 237 (1986).
[49] See Supplemental Material at http://link.aps.org/supplemental/10.1103/bwtd-x5cj for a table with the dielectric constants of both systems in each phase.
[50] www.nhr-verein.de/unsere-partner.